



Deterministically fabricated spectrally-tunable quantum dot based single-photon source

MARCO SCHMIDT, MARTIN V. HELVERSEN, SARAH FISCHBACH, ARSENTY KAGANSKIY, RONNY SCHMIDT, ANDREI SCHLIWA, TOBIAS HEINDEL,  SVEN RODT, AND STEPHAN REITZENSTEIN*

Institut für Festkörperphysik, Technische Universität Berlin, Hardenbergstraße 36, 10623 Berlin, Germany
*stephan.reitzenstein@physik.tu-berlin.de

Abstract: Spectrally-tunable quantum light sources are key elements for the realization of long-distance quantum communication. A deterministically fabricated single-photon source with a photon extraction efficiency of $\eta = (20 \pm 2) \%$, a maximum tuning range of $\Delta E = 2.5$ meV and a minimum $g^{(2)}(\tau = 0) = 0.03 \pm 0.02$ is presented. The device consists of a single pre-selected quantum dot (QD) monolithically integrated into a microlens that is bonded onto a piezoelectric actuator via gold thermocompression bonding. Here, a thin gold layer simultaneously provides strain transfer and acts as a backside mirror for the QD-microlens to maximize the photon extraction efficiency. The QD-microlens structure is patterned via 3D in-situ electron-beam lithography (EBL), which allows us to pre-select and integrate suitable QDs based on their emission intensity and energy with a spectral accuracy of 1 meV for the final device. Together with strain fine-tuning, this enables the scalable realization of single-photon sources with identical emission energy. Moreover, we show that the emission energy of the source can be stabilized to μeV accuracy by closed-loop optical feedback. Thus, the combination of deterministic fabrication, spectral-tunability and high broadband photon-extraction efficiency makes the QD-microlens single-photon source an interesting building block for the realization of quantum communication networks.

© 2019 Optical Society of America under the terms of the [OSA Open Access Publishing Agreement](#)

1. Introduction

Quantum communication protocols promise secure data transmission based on single-photon technology [1–3]. In this context, implementations of long-distance quantum key distribution require Bell-state measurements in quantum repeaters [4] to transfer quantum states between different nodes of a communication network. Two recent experiments, which demonstrate entanglement swapping of entangled photon pairs consecutively emitted by the same emitter, impressively underline the high potential of semiconductor QDs in this regard [5,6]. Beyond such proof-of-principle experiments and to enable large-scale quantum repeater networks, sources emitting at the same energy, on the order of the homogeneous linewidth of the emitters, are required in each node of the network.

Semiconductor QDs are promising candidates for such applications, as they emit photons with simultaneously close-to-ideal indistinguishability, entanglement fidelity and extraction efficiency when integrated into suitable photonic structures like circular Bragg gratings in a hybrid device design [7,8]. However, one has to note that the self-assembled Stranski-Krastanov growth mode, which is typically used to realize high-quality InGaAs QDs, leads to randomly distributed emitters with varying shape and size, resulting in an emission band with inhomogeneous broadening of typically 10-50 meV. Noteworthy, values of only a few meV have been realized for QDs grown on inverted pyramids [9], which, however, is still three orders of magnitude larger than the homogenous linewidth of the QDs. Therefore, post-growth processing is required to meet the demands of advanced photonic quantum technology. With respect to the requirement of

realizing spectrally precisely matched single-photon sources, deterministic in-situ optical and electron beam lithography techniques [10,11] allow one to pre-select and integrate bright emitters within the QD ensemble with a spectral accuracy of better than 1 meV. In combination with spectral fine-tuning, that is key to achieve spectral resonance of multiple single-photon sources within the QD's homogeneous linewidth of about 1-2 μeV , which has high potential to enable entanglement swapping between remote sources in large-scale quantum repeater networks in the future. Moreover, the precise tunability of single-photon sources is also beneficial for the coupling of single-photon emitters to other key components of advanced quantum networks, namely quantum memories, realized e.g. by atomic vapors [12], trapped atoms [13] or solid state quantum memories [14].

Various methods have been applied to achieve spectral control of the QD emission characteristics, often accompanied with drawbacks: Temperature tuning [15], for instance, suffers from increased phonon-contributions finally limiting the photon indistinguishability already above 10-15 K [16]. Electric fields can be applied to influence the QD emission via the quantum-confined Stark effect [17,18]. This scheme, however, requires complex doping and electrical contacts which complicates the device processing. Strain-tuning proved to be an excellent alternative, which can be implemented by integration of the emitter onto a piezoelectric material such as $\text{Pb}(\text{Mg}_{1/3}\text{Nb}_{2/3})\text{O}_3\text{-PbTiO}_3$ (PMN-PT) [19,20]. In addition to the spectral-tunability, strain-tuning can be used to control the exciton binding energies and the fine structure splitting of QD states, which enables the generation of polarization-entangled photon pairs [21]. In view of applications of single-photon sources in secure quantum communication scenarios, high photon extraction and collection efficiencies are desirable to achieve high data transmission rates. So far, only few attempts have been made to increase the efficiency of strain-tunable single-photon sources. In one example an extraction efficiency of 57% into a numerical aperture of 0.8 has been achieved using strain-tunable nanowire antennas [22].

In this work, we present a bright spectrally-tunable single-photon source based on a deterministically fabricated QD microlens combined with a piezoelectric actuator by a flip-chip goldbonding technique. The applied in-situ EBL technique has the important advantage that suitable QDs can be pre-selected by their emission intensity and emission energy with a spectral accuracy better than 1 meV before integrating them into photonic nanostructures. Moreover, with a positioning accuracy of about 30-40 nm [23], broadband enhancement of the photon-extraction efficiency is achieved. The mentioned uncertainty in emission energy of approximately 1 meV is attributed to different charge configurations after integration of the QD into a photonic microstructure with etched surfaces [24]. We show that piezo strain-tuning can compensate this spectral uncertainty and, thus, promises a scalable route towards large scale quantum networks based on entanglement distribution between quantum light sources with identical emission energy.

2. Device design and fabrication

The fabrication of our device involves three main processing steps: First a semiconductor heterostructure is grown by metal-organic chemical vapor deposition. Subsequently, a flip-chip gold thermocompression bonding process is applied, which results in a thin GaAs membrane including the QDs attached to the piezoelectric actuator. In a final step, single QDs are deterministically integrated into microlenses by means of in-situ EBL.

The growth process starts with an $\text{Al}_{0.97}\text{Ga}_{0.03}\text{As}$ layer with a thickness of 1 μm which is deposited on a GaAs (100) substrate, acting as an etch stop layer later on. Above this layer, 570 nm of GaAs are grown including the InGaAs QDs in a distance of 200 nm to the sample surface. The QD layer with a wafer-position dependent density of $10^8\text{-}10^9\text{ cm}^{-2}$ and an emission band with an inhomogeneous broadening of 30 meV is centered at 1.33 eV (930 nm). For the flip-chip bonding process, 200 nm of gold are deposited onto the sample using electron-beam evaporation. Additionally, a 300 nm gold layer is evaporated on a PIN-PMN-PT

($\text{Pb}(\text{In}_{1/2}\text{Nb}_{1/2})\text{O}_3\text{-Pb}(\text{Mg}_{1/3}\text{Nb}_{2/3})\text{O}_3\text{-PbTiO}_3$) crystal. This material is chosen as it has an increased depoling temperature of $T_C = 140^\circ\text{C}$ and a higher coercive field of $E_c = 6\text{ kV cm}^{-1}$ as compared to the more commonly used PMN-PT with $T_C = 90^\circ\text{C}$ and $E_c = 2.5\text{ kV cm}^{-1}$ [25]. Next, the QD sample is placed upside-down onto the piezoelectric actuator with the two gold layers facing each other (cf. Fig. 1(a)). A pressure of 6 MPa at a temperature of approximately 600 K is applied for 4 hours to achieve a strong cohesion of the gold layers.

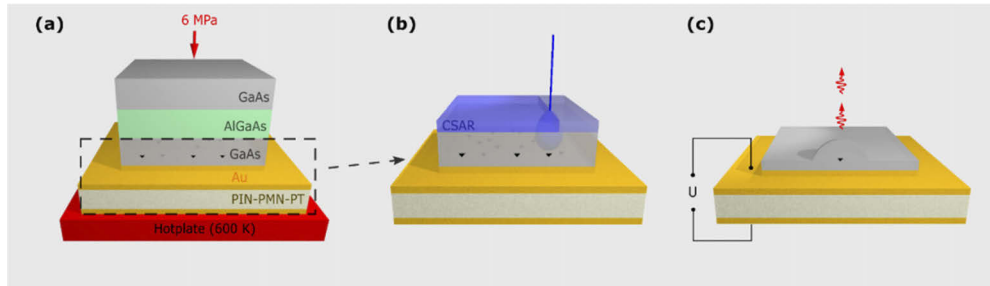


Fig. 1. Schematic illustration of the fabrication process of a tunable QD microlens: (a) Gold thermocompression bonding of the layer structure including InGaAs QDs, followed by a wet etching step to remove the GaAs substrate and the etch stop layer. (b) Mapping process for the in-situ EBL. Suitable QDs are chosen and integrated into microlens structures. (c) The PIN-PMN-PT is contacted to transfer strain to the QD microlens for spectral-tuning of the single-photon emission.

In the next step, the upper GaAs substrate is removed by a stirred solution of hydrogen peroxide and ammonium hydroxide until the etching stops at the $\text{Al}_{0.97}\text{Ga}_{0.03}\text{As}$ layer. The latter is removed by hydrochloric acid such that a semiconductor membrane with a thickness of 570 nm remains on top of the gold layer.

To enhance the photon-extraction efficiency and to pre-select bright QDs with a specific emission energy, 3D in-situ EBL at 10 K is applied. This method allows us to conveniently choose QDs with a target emission energy and high emission intensity within a scanned area of the sample by their cathodoluminescence (CL) characteristics. Figure 1(b) illustrates the CL mapping process. Sample areas of $20\ \mu\text{m} \times 20\ \mu\text{m}$ are scanned and suitable QDs are chosen. A microlens is written into the resist on top of it, which is afterwards developed such that the structure can be transferred into the GaAs top layer by reactive-ion-enhanced plasma etching. The whole selection and EBL process takes less than 10 minutes per write field, each including up to about 5 QD-microlenses, so that tens of such devices with emission at the target wavelength can be realized in a few hours. For more details on the 3D in-situ EBL process we refer to [11]. The final device is shown in Fig. 1(c). The device and lens geometry were optimized beforehand using the commercially available software-package JCMsuite by the company JCMwave, which is based on a finite-element method. The optimum lens geometry leads to a photon extraction efficiency of 42% for a numerical aperture of 0.4 and is identified as a spherical segment with a height of 370 nm and a radius of 1264 nm.

3. Micro-photoluminescence characterization

The optical properties of the final device are investigated by means of micro-photoluminescence spectroscopy under non-resonant excitation (laser wavelength: 665 nm) at a temperature of 10 K with a spectral resolution of 27 μeV . Figure 2(a) shows a spectrum of a QD microlens device (QDM1) at saturation of the excitonic lines. Excitation-power- and polarization dependent measurements are used for the assignment of the emission lines to respective quantum dot states. The most intense line at $E_{X^-} = 1.3520\text{ eV}$ is identified as a charged excitonic transition (X^-), the

transition at $E_X = 1.3536$ eV as the neutral excitonic transition (X) due to its polarization splitting of $\Delta E_{FSS} = 7$ μ eV, while a charged biexcitonic line is observed at $E_{XX^{+/-}} = 1.3490$ eV. To evaluate the photon-extraction efficiency η of the microlens device, we use a Titan-Sapphire laser ($f = 80$ MHz) to excite the QD state X^- at saturation and detect the emitted photons using a calibrated experimental setup (cf. Experimental Section). At zero bias voltage applied to the piezo element we observe $\eta(X^-) = (17 \pm 2)\%$ for the charged excitonic transition with a linewidth of 46 μ eV (FWHM). This value is smaller than 42% expected for an optimized spherical microlens, where the deviation is mainly attributed to the nonideal shape of the realized structure with noticeable surface roughness and a rather flat top. Indeed, a micromesa with similar geometry would yield a photon extraction efficiency of 18% [26]. Thus, further work needs to focus on a more precise lithography and processing of spherical microlenses or circular Bragg reflectors on top of a gold bonded structure to enhance the extraction efficiency.

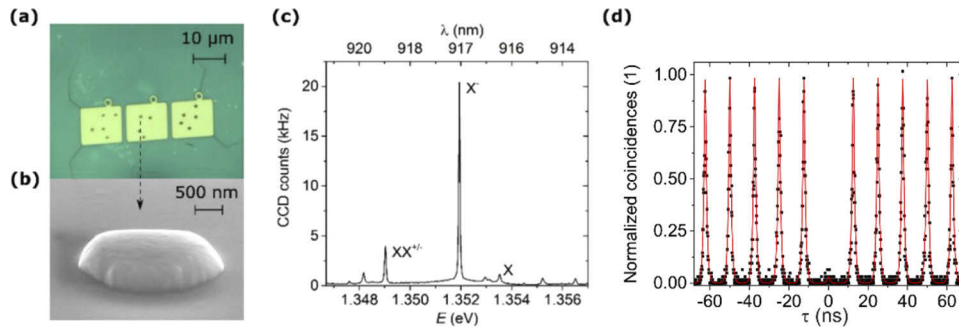


Fig. 2. (a) Microscope image of CL map areas taken during in-situ EBL with QD microlenses. (b) Scanning electron microscope image of a microlens. (c) Micro-photoluminescence spectrum of a QD microlens (QDM1) at $T = 10$ K. (d) Photon-autocorrelation measurements stating single-photon emission with $g^{(2)}(\tau=0) = 0.03 \pm 0.02$.

Next, we verify the single-photon emission of our spectrally-tunable microlens device under pulsed wetting-layer excitation at $\lambda = 897$ nm. The photon-autocorrelation measurement at saturation of the X^- line in Fig. 2(d) shows pronounced antibunching at $\tau = 0$. To quantitatively evaluate the suppression of multi-photon emission events, the experimental data was fitted with a sequence of equidistant two-sided exponential functions

$$g^{(2)}(\tau) = \left(p_0 e^{-\frac{|\tau|}{t_d}} + p_t \sum_{\substack{i=-5 \\ i \neq 0}}^5 e^{-\frac{|\tau - \frac{i}{f}|}{t_d}} \right) \otimes G(\tau, \sigma_{\text{res}})$$

with decay time t_d convoluted with a Gaussian $G(\tau)$ with $\sigma_{\text{res}} = 300$ ps / $2\sqrt{2\ln 2}$ width, accounting for the timing resolution of the Hanbury-Brown and Twiss setup.

The ratio of the peak amplitudes at zero-time delay p_0 and at finite time delays p_t reveals the second-order photon-autocorrelation value $g^{(2)}(\tau = 0) = 0.03 \pm 0.02$ ($t_d = (0.69 \pm 0.01)$ ns). These results confirm that our advanced multi-step device processing enables the realization of bright single-photon sources with a high suppression of multi-photon emission events.

4. Strain-tunability of single-photon emission

To demonstrate the spectral tunability of QD emission, a voltage of -600 to $+600$ V is applied to the PIN-PMN-PT material, corresponding to an electric field F of -20 to $+20$ kVcm^{-1} . A positive (negative) voltage corresponds to an in-plane compression (extension) of the piezoelectric crystal transferred to the semiconductor material and the QD layer. Using the full tuning range results in a shift of the X^- emission by $\Delta E = 2.5$ meV as shown in Fig. 3(a).

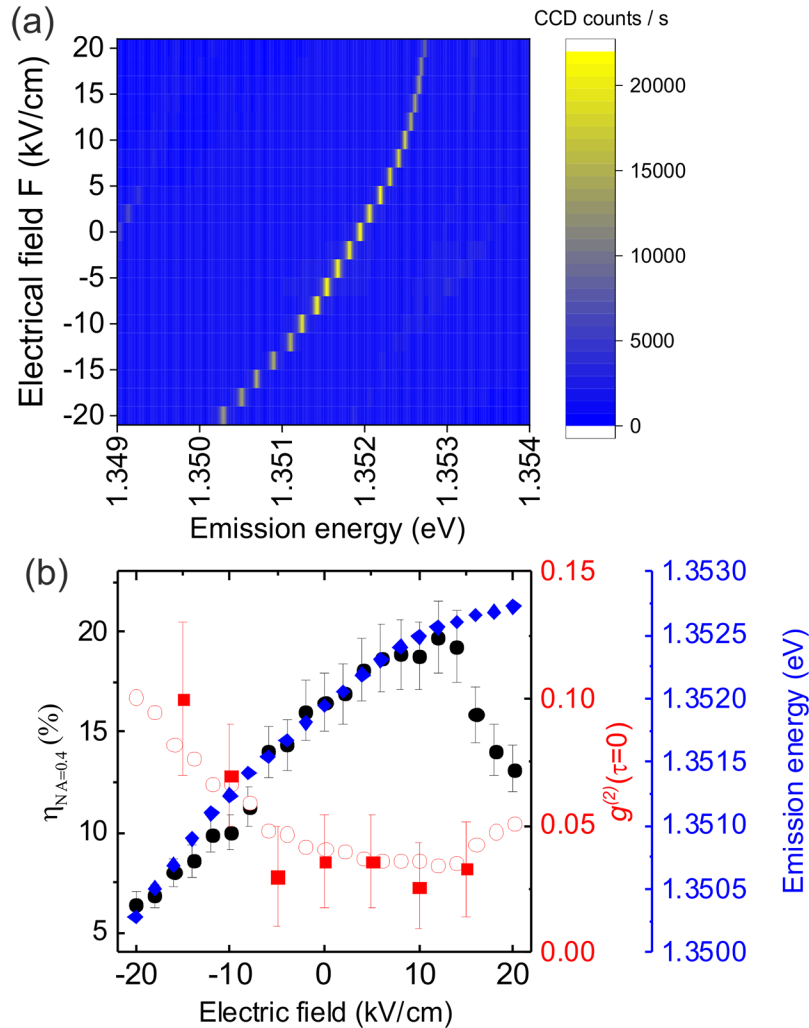


Fig. 3. (a) Energy tuning of the X^- emission line of QDM1 by application of an electric field F to the piezoelectric actuator. (b) Extraction efficiency (black, left axis), equal-time second-order photon autocorrelation ($g^{(2)}(\tau=0)$) results (red squares, right axis) and calculated $g^{(2)}(\tau=0)$ taking the F -dependent extraction efficiency into account (red circles, right axis). X^- emission energy for the full tuning range (blue, right axis).

Besides the tunability of the emission energy, Fig. 3(a) also reveals a change in the emission intensity with the applied electric field, which we further investigated by measuring the photon

extraction efficiency in pulsed excitation. As can be found in Fig. 3(b), the highest efficiency is achieved at an applied field of $F_{\max} = 12 \text{ kV cm}^{-1}$ with $\eta(X^-, F_{\max}) = (20 \pm 2)\%$. The efficiency decreases down to $\eta(X^-, F_{\min}) = (6 \pm 1)\%$ at the lowest field value $F_{\min} = -20 \text{ kV cm}^{-1}$. Additionally, we investigated the second-order photon autocorrelation function for different detunings. The suppression of multi-photon emission events $g^{(2)}(\tau = 0)$ remains constant and below 0.05 over a wide tuning range and increases at high negative electric fields to $g^{(2)}(0) = 0.10 \pm 0.03$ at $F = -15 \text{ kV cm}^{-1}$. The associated X^- emission energy plotted in blue shows that we can obtain an effective tuning range of about 1 meV in which high extraction efficiency $> \approx 15\%$ and high multi-photon suppression with $g^{(2)}(0) < 0.05$ can be achieved. This tuning range covers well the in-situ EBL spectral accuracy so that a combination of both enables the scalable realization of SPS with identical emission energy as we demonstrate in the next section. An increased $g^{(2)}(0)$ can be explained by a decrease of the signal (S) to uncorrelated background (B) ratio. To support this statement we consider $g^{(2)}(\tau) = 1 + \rho^2(g_{\text{BF}}^{(2)}(\tau) - 1)$, with $\rho = S/(S + B)$ and the background free value $g_{\text{BF}}^{(2)}(\tau)$ [27], to describe the field dependence of $g^{(2)}(0)$. A direct connection to the photon extraction efficiency is obtained by taking into account that S is proportional to the measured extraction efficiency (black data points in Fig. 3(b)) and that a constant uncorrelated background contribution of η_B is present which leads to $g^{(2)}(\tau) = 1 + (\eta_{\text{Device}}/(\eta_{\text{Device}} + \eta_B))^2(-1)$. Under the assumption that the background free $g_{\text{BF}}^{(2)}(0)$ is zero. Very good agreement between experimental data (red squares in Fig. 3(b)), with $\eta_{\text{Device}} = \eta_{\text{NA}=0.4}$ and the calculated values (open red circles in Fig. 3(b)) is obtained for $\eta_B = 0.0035$, which supports our interpretation of a signal-to-background dependent increase of $g^{(2)}(0)$ for negative F . The strain influence on the extraction efficiency could be connected to electric fields caused by charge states on the surface of the microlens. The charge states create a field distribution around the QD which depends on the external strain. Previous studies showed that the processing of microstructures by in-situ EBL gives a lateral positioning accuracy of 34 nm [23]. Such a deviation from the center could be sufficient for the QD to be influenced by the mentioned strain-induced electric field distribution, leading to a slight separation of the electron and hole wavefunction, which in return can reduce the emission rate as we observe in the experiment. Measurements of the decay time of the QD X^- emission yield a value of approximately 0.65 ns, which is not significantly influenced by the electric field F applied to the piezo actuator, the rise time increases from about 200 ps to 350 ps with decreasing F below zero. This change of rise time could indicate a lower capture probability in agreement with the reduced photon extraction efficiency in this field range. A more detailed description would require a detailed knowledge of the QD position in the microlens which is beyond the scope of the present work.

To demonstrate the scalability of our device concept, we evaluated the strain-tuning behavior of four additional QD-microlenses QDM2-5 which were fabricated together with QDM1 on the same sample with the same target emission energy. In Fig. 4 the excitonic emission energies of these microlenses are plotted relative to the X^- emission of QDM1 as function of the electric field applied to the piezo actuator. The emission energy of all four lenses can be tuned through resonance with the emission energy of QDM1 (indicated by the dashed line). This feature will be very helpful in future experiments aiming at entanglement swapping between remote QD-SPSS. The fact that spectral resonance between the five sources cannot be achieved at the same electric field is not relevant for this application, for which the sample could either be split or different samples with the same target emission energy could be realized by in-situ EBL.

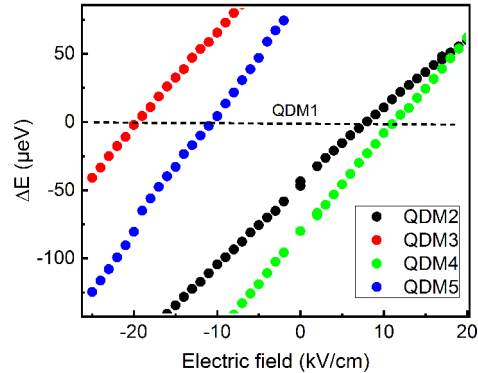


Fig. 4. Strain-tuning of four QD microlenses (QDM2-5) which were deterministically fabricated together with device QD1 on the same piece of sample. The excitonic emission energies of these QDM2-5 microlenses are plotted relative to the X^- emission energy of QDM1. They can be tuned through resonance with QD microlens QDM1 by applying suitable electrical fields between about -20 kVcm^{-1} and 10 kVcm^{-1} to the piezo actuator.

5. Theoretical analysis of strain-transfer and strain-tuning of QD structures

To further analyze the effects of the external strain we compare our measurements to results obtained by theoretical modeling of the microlens device. The additional strain exerted by the piezoelectric actuator is accounted for by adjusting the lattice constant a_0 of the lowest GaAs layer above the gold mirror to $\tilde{a} = a_0 - c \cdot a_0$, and the strain distribution inside the full GaAs device is calculated in the framework of continuum elasticity. One has to distinguish between the permanent strain caused by the inherent lattice mismatch between the GaAs substrate and the InGaAs QD, and the effects of the external strain caused by the piezo-tuning. Moreover, the hydrostatic strain component can be separated from the biaxial strain component. Figure 5 shows the calculation results for the permanent strain without external influence ((a1) and (b1)) as well as the additional strain effects induced by an applied external compressive as well as tensile strain ((a2) and (b2)). The distribution across the lens structure is almost uniform, only a slight relaxation effect is visible for the hydrostatic strain component as compared to the planar area around the lens. Possible shear strain was not taken into account in the simulations, because this would add a complexity to the calculation that is outside of the scope of this work.

Applied strain may affect the energies of the localized electronic states via (i) deformation potentials, thus, changing the local band positions, (ii) the alteration of the quantization energies, and (iii) the change in electron-hole Coulomb interaction. Careful analysis using eight-band k-p theory together with the configuration interaction method [28], however, revealed that effect (i) constitutes the governing contribution, whereas (ii) and (iii) are only minor contributions, which are neglected in the following discussion. The achieved tuning of $\Delta E = 2.5 \text{ meV}$ corresponds to a change in the lattice constant of $c = \pm 1.2 \cdot 10^{-3}$ for compressive (+) and tensile (-) strain. At the position of the QD the resulting sum of the relative hydrostatic and biaxial strain components in all three directions are calculated separately to $\Delta\epsilon_{\text{hy}}(c) = \pm 8.1 \cdot 10^{-4}$ and $\Delta\epsilon_{\text{biax}}(c) = \pm 4.65 \cdot 10^{-3}$, where the hydrostatic strain is responsible for band-shifts and the biaxial strain for the heavy-hole light-hole splitting [29]. The sum of both effects is driving the change in the luminescence energy. Combined with the deformation potentials in $\text{In}_{0.7}\text{Ga}_{0.3}\text{As}$, $a_g = -6725.9 \text{ meV}$ for the hydrostatic

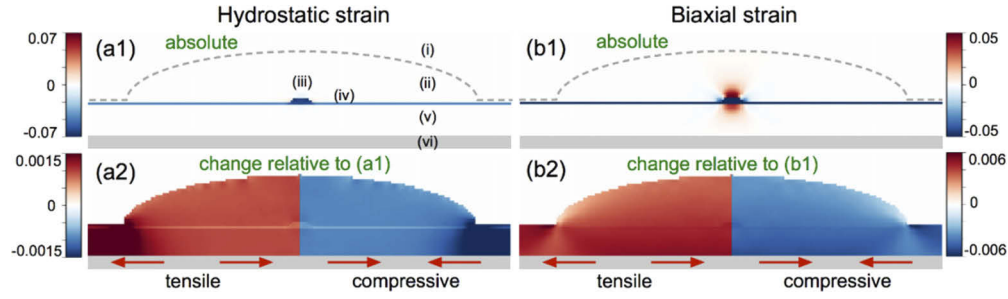


Fig. 5. Calculated hydrostatic (a1/a2) and biaxial (b1/b2) strain distributions in a QD microlens. (a1/b1) refer to the situation in absence of external strain, while (a2) and (b2) show the additional effects by external tensile (left) and compressive strain (right). The domain is divided into (i) air, (ii) lens, (iii) QD, (iv) wetting layer, (v) spacer layer, and (vi) the piezoelectric actuator. Red (blue) color indicates the relative tensile (compressive) strain.

strain and $b_v = -1897.2$ meV for the biaxial strain, the energy shift can be calculated as

$$\Delta E(c) = a_g(\Delta\epsilon_{hy}(c)) - \frac{1}{2}b_v(\Delta\epsilon_{biac}(c)) = \pm 1.25 \text{ meV}.$$

Using the piezoelectric coefficient $d_{31} \approx 1500$ pC N⁻¹ as published by the manufacturer (CTS Corporation), we can compare the theoretically evaluated strain with the experimentally applied value. The maximum strain that is induced in one lateral direction during the measurement can be estimated to

$$\epsilon^{\text{exp}} = d_{31} \cdot F_{\text{max}} = 1500 \text{ pC N}^{-1} \cdot 20 \text{ kV cm}^{-1} = 3 \cdot 10^{-3},$$

as compared to the theoretical value of $c = 1.2 \cdot 10^{-3}$. Matching the calculation results with the achieved tuning, it can be estimated that a fraction of $\frac{c}{\epsilon^{\text{exp}}} = 40$ % of the strain effect at the piezoelectric crystal is transferred to the position of the studied QD.

6. Closed-loop stabilization of emission energy

A critical aspect of our target application in quantum communication networks is the long-term spectral stability of our energy-tunable SPSs. In this regard the well-known creep behavior of piezoelectric actuators is a severe issue [30]. To illustrate this point, the time-dependence of the emission energy of another strain-tunable QD-microlens device is presented in Fig. 6(a), where the electric field was changed up from zero to 12 kVcm⁻¹ at time $t = 0$. In the first 30 minutes of the measurement series, the emission energy increased rather strongly by about 350 μeV . Subsequently, in the next 120 minutes a further linear blue-shift of about 30 μeV took place because of the typical creeping behavior of the piezo-materials, before the emission finally approaches a stable value. Thus, for applications requiring large tuning ranges, a stabilization time of approximately 3 hours needs to be considered before stable operation of the SPS in this open-loop scenario. Moreover, even in the ‘stable state’ creep related spectral shifts on the order of several μeV do occur, preventing the implementation of entanglement swapping which requires sub- μeV spectral stability.

To improve the strain-tuning behavior and the long-term spectral stability of our devices we implemented an active feedback loop with a proportional–integral–derivative (PID) controller. We use an experimental approach similar that reported in Ref. [20]. Essentially, in this rather straight-forward approach the signal emitted by the QD-microlens is coupled to a spectrometer at adjustable time intervals of typically a few ten seconds to monitor the emission wavelength

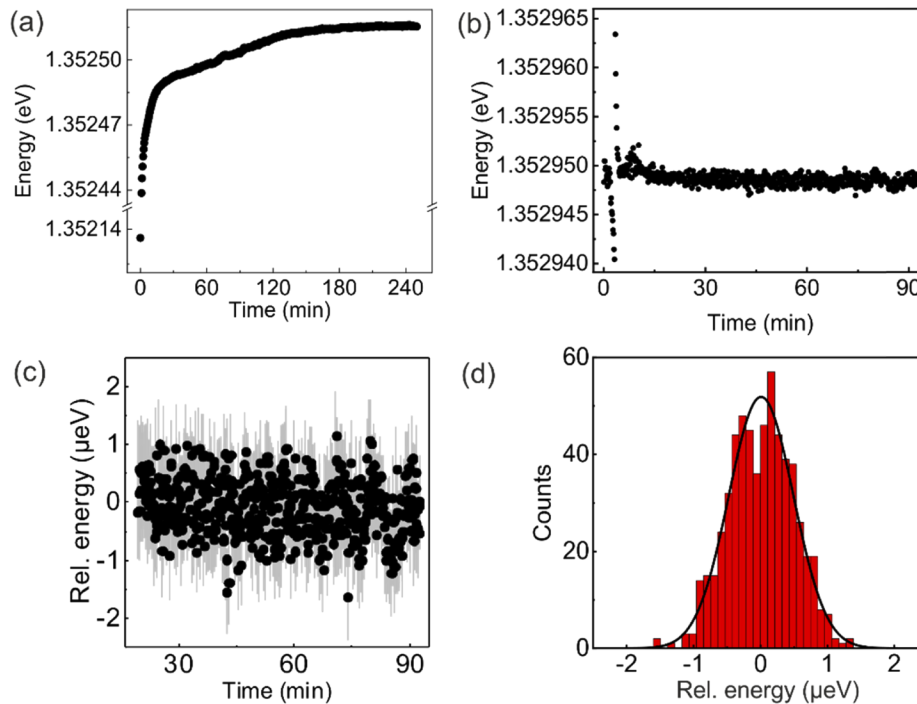


Fig. 6. (a) Time series of the excitonic emission energy of a QD-microlens after changing the piezo field from zero to $F = 12 \text{ kV cm}^{-1}$ at time $t = 0$ in open-loop configuration. (b) Time-dependence of emission energy in closed loop configuration using an active optical feedback control. The jump in intensity at $t = 2$ min was caused by an intentional perturbation of the system. (c) Zoom-in view of the emission energy relative to the set point (error bars in shaded grey). (d) Corresponding histogram of relative emission energies with a standard deviation of $0.5 \text{ } \mu\text{eV}$.

with a spectral accuracy of $0.8\text{-}1.0 \text{ } \mu\text{eV}$ with an integration time between few tens milli-seconds and few seconds depending on the signal strengths. We installed a short (1 m) single-mode fiber section in the detection path before focusing the optical signal to the input slit of the spectrometer. This fiber section is crucial to enhance the spectral accuracy of the implemented control loop, as small angle deviations of the detection beam path change the position of the emission line on the spectrometer's CCD, thus preventing a reliable detection of the emission energy with the required accuracy. Within a PID control loop with optical feedback, the center energy of the target emission line is determined in each iteration by Lorentzian fitting of the detected spectrum and is compared to the setpoint energy. In case of deviations from the target energy, the voltage output to the piezo actuator is readjusted to shift the emission line back to the setpoint via adapted strain. To ensure best performance of the control loop, the optimum PID parameters are determined by the pulse response of the system.

To illustrate the functionality of the described control-loop we stabilized the emission energy of a QD-microlens to a setpoint of 1.3529485 eV . Figure 6(b) shows the corresponding time evolution of the feedback-controlled center energy for a time period of approximately 90 minutes. The jump at $t = 2$ min marks an intentional (mechanical) perturbation, to test the dynamic response of the control loop. Within a characteristic dynamic response time of about minutes, the emission energy returns to the setpoint. Subsequently, the emission energy is stabilized efficiently by the control-loop as can be seen in the zoom-in view of the emission energy relative to the setpoint. The data yields a standard deviation as low as $0.5 \text{ } \mu\text{eV}$ ($1.2 \text{ } \mu\text{eV}$ FWHM) as shown

by the corresponding histogram (obtained for the time range of 7 to 90 minutes) in Fig. 6(d). Importantly, this value compares well with the typical homogenous linewidth (approximately 1-2 μeV) of the InGaAs QDs under study and, thus, can pave the way for future entanglement swapping experiments between remote quantum light sources.

7. Experimental section

7.1. *In-situ electron beam lithography*

With the in-situ EBL step, QDs are chosen by their cathodoluminescence (CL) signal and integrated into microlens structures. The samples are prepared by spin-coating with the electron-beam resist AR-P 6200 (CSAR 62) and mounted onto the cold finger of a He-flow cryostat of a customized scanning electron microscope for low-temperature operation at 10 K. The reaction of the resist during development depends on the applied electron dose during exposure. This resist has a positive-tone regime at low electron doses, which are used for mapping of the CL signal. The luminescence signal is focused into a monochromator and detected with a Si charge-coupled device camera. Based on that data, QDs are chosen and microstructures are written into the resist above them with a higher electron dose. Above a certain threshold value, the resist enters a negative tone regime, such that the structures remain after development. The transition range to the complete negative-tone regime is used to create quasi-3D designs (see Ref. [11] for details). Finally, dry etching is performed by inductively-coupled-plasma reactive-ion etching.

7.2. *Optical measurements*

The sample is mounted in a helium-flow cryostat and cooled down to 10 K. It is optically excited using a Titan-Sapphire laser that can be operated in quasi-continuous wave (CW) or pulsed ($f = 80$ MHz) mode. The photoluminescence is collected using a microscope objective with an NA of 0.4 and spectrally dispersed by a grating monochromator, before it is detected using a Si charge-coupled device camera. The setup is also equipped with a fiber-coupled Hanbury-Brown and Twiss setup using single-photon counting modules based on Si avalanche photo diodes. To evaluate the extraction efficiency into the first lens of our experimental setup, the transmission of the complete setup was measured to be $\eta_{\text{Setup}} = (1.1 \pm 0.1) \%$ following the procedure described in Ref. [11]. Using a laser with repetition rate f a detected count-rate n_{QD} corresponds to a photon-extraction efficiency of $\eta_{\text{Device}} = \frac{n_{\text{QD}}}{\eta_{\text{Setup}} * f}$. Furthermore, the photon extraction efficiency is defined as $\eta_{\text{Device}} = \eta_{\text{geo}} \eta_{X^-}$, where η_{geo} denotes the purely geometrical contribution to the photon extraction efficiency of the device, while η_{X^-} the probability of emitting a photon by the X^- per excitation pulse. The latter includes the occupation probability and the quantum efficiency of this QD transition, which can be influenced by the applied mechanical strain under non resonant excitation.

8. Conclusion

In conclusion, we presented a spectrally-tunable single-photon source with a maximum photon extraction efficiency of $\eta = (20 \pm 2) \%$ and a total tuning range of $\Delta E = 2.5$ meV. This tuning range is reduced to about 1 meV when focusing on an operation regime of $\eta > 15\%$ and $g^{(2)}(0) < 0.05$. The emission energy of our device is pre-selected with an accuracy of about 1 meV by using in-situ EBL applied to a planar sample bonded onto a piezoelectric actuator via flip-chip gold thermocompression bonding. In addition, a feedback-loop is implemented which enables locking the emission energy with a standard deviation of 0.5 μeV (FWHM: 1.2 μeV). Thus, the achieved effective tuning can serve to adjust the emission to meet the exact transition energy required e.g. for entanglement distribution in multi-node quantum networks or for the interfacing of QD based single-photon sources with quantum memories.

Funding

Bundesministerium für Bildung und Forschung (03V0630, 13N14876); Deutsche Forschungsgemeinschaft (Re2974/8-1, SFB787); Horizon 2020 Framework Programme (MIQC2, SIQUST).

Disclosures

The authors declare no conflicts of interest.

References

1. C. H. Bennett and G. Brassard, "Quantum cryptography: Public key distribution and coin tossing," *Proc. of IEEE International Conference on Computers, Systems and Signal Processing*, 175 (1984).
2. A. K. Ekert, "Quantum cryptography based on Bell's theorem," *Phys. Rev. Lett.* **67**(6), 661–663 (1991).
3. N. Gisin and R. Thew, "Quantum communication," *Nat. Photonics* **1**(3), 165–171 (2007).
4. H.-J. Briegel, W. Dür, J. I. Cirac, and P. Zoller, "Quantum Repeaters: The Role of Imperfect Local Operations in Quantum Communication," *Phys. Rev. Lett.* **81**(26), 5932–5935 (1998).
5. F. Basso Basset, M. B. Rota, C. Schimpf, D. Tedeschi, K. D. Zeuner, S. F. C. da Silva, M. Reindl, V. Zwiller, K. D. Jöns, A. Rastelli, and R. Trotta, "Entanglement swapping with photons generated on demand by a quantum dot," arxiv:1901.06646 (2019).
6. M. Zopf, R. Keil, Y. Chen, J. Yang, D. Chen, F. Ding, and O. G. Schmidt, "Entanglement Swapping with Semiconductor-generated Photons," arxiv:1901.07833 (2019).
7. H. Wang, H. Hu, T.-H. Chung, J. Qin, X. Yang, J.-P. Li, R.-Z. Liu, H.-S. Zhong, Y.-M. He, X. Ding, Y.-H. Deng, Q. Dai, Y.-H. Huo, S. Höfling, C.-Y. Lu, and J.-W. Pan, "On-demand semiconductor source of entangled photons which simultaneously has high fidelity, efficiency, and indistinguishability," *Phys. Rev. Lett.* **122**(11), 113602 (2019).
8. J. Liu, R. Su, Y. Wei, B. Yao, S. F. C. da Silva, Y. Yu, J. Iles-Smith, K. Srinivasan, A. Rastelli, J. Li, and X. Wang, "A solid-state source of strongly entangled photon pairs with high brightness and indistinguishability," *Nat. Nanotechnol.* **14**(6), 586–593 (2019).
9. A. Surrente, M. Felici, P. Gallo, B. Dwir, A. Rudra, G. Biasiol, L. Sorba, and E. Kapon, "Ordered systems of site-controlled pyramidal quantum dots incorporated in photonic crystal cavities," *Nanotechnology* **22**(46), 465203 (2011).
10. A. Dousse, L. Lanco, J. Szczyński, E. Semenova, A. Miard, A. Lemaître, I. Sagnes, C. Roblin, J. Bloch, and P. Senellart, "Controlled Light-Matter Coupling for a Single Quantum Dot Embedded in a Pillar Microcavity Using Far-Field Optical Lithography," *Phys. Rev. Lett.* **101**(26), 267404 (2008).
11. M. Gschrey, A. Thoma, P. Schnauber, M. Seifried, R. Schmidt, B. Wohlfeil, L. Krüger, J.-H. Schulze, T. Heindel, S. Burger, F. Schmidt, A. Strittmatter, S. Rodt, and S. Reitzenstein, "Highly indistinguishable photons from deterministic quantum-dot microlenses utilizing three-dimensional in situ electron-beam lithography," *Nat. Commun.* **6**(1), 7662 (2015).
12. K. S. Choi, H. Deng, J. Laurat, and H. J. Kimble, "Mapping photonic entanglement into and out of a quantum memory," *Nature* **452**(7183), 67–71 (2008).
13. H. P. Specht, C. Nölleke, A. Reiserer, M. Uphoff, E. Figueroa, S. Ritter, and G. Rempe, "A single-atom quantum memory," *Nature* **473**(7346), 190–193 (2011).
14. A. Tiranov, J. Lavoie, A. Ferrier, P. Goldner, V. Verma, S. Nam, R. Mirin, A. Lita, F. Marsili, H. Herrmann, C. Silberhorn, N. Gisin, M. Afzelius, and F. Bussièrès, "Storage of hyperentanglement in a solid-state quantum memory," *Optica* **2**(4), 279 (2015).
15. T. Farrow, P. See, A. J. Bennett, M. B. Ward, P. Atkinson, K. Cooper, D. J. P. Ellis, D. C. Unitt, D. A. Ritchie, and A. J. Shields, "Single-photon emitting diode based on a quantum dot in a micro-pillar," *Nanotechnology* **19**(34), 345401 (2008).
16. A. Thoma, P. Schnauber, M. Gschrey, M. Seifried, J. Wolters, J.-H. Schulze, A. Strittmatter, S. Rodt, A. Carmele, A. Knorr, T. Heindel, and S. Reitzenstein, "Exploring Dephasing of a Solid-State Quantum Emitter via Time- and Temperature-Dependent Hong-Ou-Mandel Experiments," *Phys. Rev. Lett.* **116**(3), 033601 (2016).
17. A. J. Bennett, R. B. Patel, J. Skiba-Szymanska, C. A. Nicoll, I. Farrer, D. A. Ritchie, and A. J. Shields, "Giant Stark effect in the emission of single semiconductor quantum dots," *Appl. Phys. Lett.* **97**(3), 031104 (2010).
18. C. Kistner, T. Heindel, C. Schneider, A. Rahimi-Iman, S. Reitzenstein, S. Höfling, and A. Forchel, "Demonstration of strong coupling via electro-optical tuning in high-quality QD-micropillar systems," *Opt. Express* **16**(19), 15006 (2008).
19. F. Ding, R. Singh, J. D. Plumhof, T. Zander, V. Křápek, Y. H. Chen, M. Benyoucef, V. Zwiller, K. Dörr, G. Bester, A. Rastelli, and O. G. Schmidt, "Tuning the Exciton Binding Energies in Single Self-Assembled InGaAs/GaAs Quantum Dots by Piezoelectric-Induced Biaxial Stress," *Phys. Rev. Lett.* **104**(6), 067405 (2010).
20. R. Trotta, P. Atkinson, J. D. Plumhof, E. Zallo, R. O. Rezaev, S. Kumar, S. Baunack, J. R. Schröter, A. Rastelli, and O. G. Schmidt, "Nanomembrane quantum-light-emitting diodes integrated onto piezoelectric actuators," *Adv. Mater.* **24**(20), 2668–2672 (2012).

21. R. Trotta, J. Martín-Sánchez, J. S. Wildmann, G. Piredda, M. Reindl, C. Schimpf, E. Zallo, S. Stroj, J. Adlinger, and A. Rastelli, "Wavelength-tunable sources of entangled photons interfaced with atomic vapours," *Nat. Commun.* **7**(1), 10375 (2016).
22. P. E. Kremer, A. C. Dada, P. Kumar, Y. Ma, S. Kumar, E. Clarke, and B. D. Gerardot, "Strain-tunable quantum dot embedded in a nanowire antenna," *Phys. Rev. B* **90**(20), 201408 (2014).
23. M. Gschrey, R. Schmidt, J.-H. Schulze, A. Strittmatter, S. Rodt, and S. Reitzenstein, "Resolution and alignment accuracy of low-temperature in situ electron beam lithography for nanophotonic device fabrication," *J. Vac. Sci. Technol., B: Nanotechnol. Microelectron.: Mater. Process., Meas., Phenom.* **33**(2), 021603 (2015).
24. A. Kaganskiy, M. Gschrey, A. Schlehahn, R. Schmidt, J.-H. Schulze, T. Heindel, A. Strittmatter, S. Rodt, and S. Reitzenstein, "Advanced in-situ electron-beam lithography for deterministic nanophotonic device processing," *Rev. Sci. Instrum.* **86**(7), 073903 (2015).
25. J. Tian and P. Han, "Crystal growth and property characterization for PIN-PMN-PT ternary piezoelectric crystals," *J. Adv. Dielectr.* **04**(01), 1350027 (2014).
26. S. Fischbach, A. Kaganskiy, E. B. Y. Tauscher, F. Gericke, A. Thoma, R. Schmidt, A. Strittmatter, T. Heindel, S. Rodt, and S. Reitzenstein, "Efficient single-photon source based on a deterministically fabricated single quantum dot - microstructure with backside gold mirror," *Appl. Phys. Lett.* **111**(1), 011106 (2017).
27. P. Michler, A. Imamoglu, A. Kiraz, C. Becher, M. D. Mason, P. J. Carson, G. F. Strouse, S. K. Buratto, W. V. Schoenfeld, and P. M. Petroff, "Nonclassical radiation from a single quantum dot," *Phys. Status Solidi B* **229**(1), 399–405 (2002).
28. A. Schliwa, M. Winkelkemper, and D. Bimberg, "Few-particle energies versus geometry and composition of $\text{In}_x\text{Ga}_{1-x}\text{As}/\text{GaAs}$ self-organized quantum dots," *Phys. Rev. B* **79**(7), 075443 (2009).
29. A. Schliwa, M. Winkelkemper, and D. Bimberg, "Impact of size, shape, and composition on piezoelectric effects and electronic properties of $\text{In}(\text{Ga})\text{As}/\text{GaAs}$ quantum dots," *Phys. Rev. B* **76**(20), 205324 (2007).
30. S. Vieira, "The behavior and calibration of some piezoelectric ceramics used in the STM," *IBM J. Res. Dev.* **30**(5), 553–556 (1986).